

PAPER

Critical role of current-driven instabilities for ELMs in NSTX

To cite this article: A. Kleiner *et al* 2022 *Nucl. Fusion* **62** 076018

View the [article online](#) for updates and enhancements.

You may also like

- [Effects of resonant magnetic perturbations on radial electric fields in DIII-D tokamak](#)
Jingyuan FU, Pengfei LIU et al.
- [Plasma performance and operational space without ELMs in DIII-D](#)
C Paz-Soldan and the DIII-D Team
- [Modifications to the edge radial electric field by angular momentum injection in JT-60U and their implication for pedestal transport](#)
K. Kamiya, M. Honda, N. Miyato et al.

Critical role of current-driven instabilities for ELMs in NSTX

A. Kleiner^{1,*} , N.M. Ferraro¹ , G. Canal², A. Diallo¹ 
and R. Maingi¹ 

¹ Princeton Plasma Physics Laboratory, PO Box 451, Princeton, NJ 08543-0451, United States of America

² Instituto de Física, Universidade de São Paulo, São Paulo CEP 05508-090, Brazil

E-mail: akleiner@pppl.gov

Received 3 January 2022, revised 31 March 2022

Accepted for publication 6 April 2022

Published 2 May 2022



Abstract

The impact of different extended-magnetohydrodynamic (MHD) contributions on the stability thresholds of peeling-ballooning modes in ELMing and ELM-free plasmas in the spherical tokamak NSTX is investigated with the initial value code M3D-C1. We show that ELMing discharges in NSTX are limited by resistive current-driven peeling modes, whereas non-ELMing wide-pedestal H-mode discharges are located near the ideal pressure-driven ballooning threshold. It is demonstrated that extended-MHD can lead to more reliable edge stability predictions than existing ideal-MHD models. Resistive peeling-ballooning modes are found to exist well before the ideal stability threshold is met, and kink-peeling modes exhibit considerable sensitivity to plasma resistivity. Other effects not considered in ideal-MHD models affect PB modes in NSTX in a weaker way. Gyroviscous stress appears stabilizing such that the stability boundary lies closer to the experimental point. Equilibrium rotation can suppress ideal core modes and thus isolate edge modes. These results are important for the development of a predictive pedestal model for low-aspect ratio tokamaks.

Keywords: magnetohydrodynamics, NSTX, peeling-ballooning, edge localized modes, ELM, pedestal, spherical tokamak

(Some figures may appear in colour only in the online journal)

1. Introduction

Characteristic for high-confinement mode (H-mode) [1] operation in tokamaks is the formation of an edge transport barrier (edge pedestal), a narrow region in which plasma density and temperature decrease sharply. This is connected with periodic sudden relaxations of the edge pressure gradient termed edge localized modes (ELMs), which cause expulsion of particles and heat [2] to the plasma facing components. ELMs not only limit the performance of present day tokamaks, but due to the dangerous heat load levels on plasma facing components [3] are a major challenge for reactor scale devices. Different types of ELMs have been observed and classified based on the dependence of their repetition frequency and amplitude on heating power. Type-I ELMs are typically considered to be the most dangerous kind [4].

* Author to whom any correspondence should be addressed.

The peeling-ballooning (PB) model [5, 6] provides an understanding of ELMs in terms of macroscopic magnetohydrodynamic (MHD) instabilities, where (higher- n) ballooning modes are driven by the large pressure gradient and peeling modes (low- n) by the bootstrap current at the edge pedestal [7, 8]. This ideal MHD model is capable of well capturing the stability thresholds in conventional aspect ratio devices. However, it was found that in spherical tokamaks (STs) this model can be less reliable. While in past studies ELMing discharges in MAST have been found to be limited by ideal ballooning modes [9, 10], this is not the case for NSTX. Here, ideal PB mode stability thresholds can be strongly underestimated, such that ELMing plasmas are predicted to sit deep inside the stable domain [11–15]. STs are characterized by a smaller size, higher normalized pressure, and higher bootstrap current [16] fraction compared with conventional aspect ratio devices, and

thus are promising candidates for economically viable fusion reactors [17, 18]. Understanding the occurrence of ELMs in STs is crucial for the development of future low aspect ratio tokamaks. A reason for the inaccurate PB predictions in low aspect ratio plasmas could be the limitation to ideal-MHD. It is known that resistivity can expand the unstable domain of ideal MHD modes, for example resistive ballooning modes [19, 20] are unstable in the first region of stability (at low pressure) of ideal ballooning modes.

Studies of non-ideal MHD effects on PB modes have been carried out for simple toroidal configurations [21] where the exact experimental configuration (low-aspect ratio, shaping and the presence of an X-point) were not taken into account. A shift of the PB stability threshold at realistic plasma resistivity in ELMing NSTX discharges was described in recent work [22]. The goal of the present paper is to provide a more detailed understanding of resistive edge stability limits in NSTX, and to show the influence of other non-ideal effects such as gyroviscosity and plasma rotation on PB mode stability. This is done in terms of linear stability simulations with the extended-MHD code M3D-C1 [23–25].

The analysis takes into account multiple ELMing and non-ELMing scenarios in NSTX with weak and strong shaping. We consider standard H-mode with type-I ELMs and ELM-free wide-pedestal H-mode (WP H-mode) [18] cases. An ELMing discharge in DIII-D is used to compare the characteristics of resistive PB mode eigenfunctions in NSTX with those described by ideal-MHD in conventional aspect ratio. In our study it is shown that plasma resistivity crucially alters PB stability thresholds in ELMing NSTX discharges, thus providing a consistent picture between multiple experiments and theoretical calculations for the first time. It is observed that ELMing NSTX discharges are limited by current-driven kink-peeling modes, which are sensitive to plasma resistivity. This can explain why ideal-MHD often does not accurately capture the stability thresholds in NSTX. Other considered non-ideal effects have a weak or moderate effect on stability, and can provide more realistic PB stability boundaries. Surprisingly, it is also found that NSTX discharges sitting on or near the ballooning (pressure-driven) stability threshold do not exhibit ELMs, suggesting that it is the current-driven instabilities alone that are responsible for ELMs in NSTX. These findings can contribute to the development of an EPED-like predictive pedestal structure model, which is important for the path towards a compact fusion power plant.

This paper is structured as follows: section 2 explains the calculation of the stability boundary with extended-MHD models implemented in the M3D-C1 code, and shows the experimental equilibria used in the simulations. Section 3 investigates the effect of resistivity on macroscopic edge stability in ELMing and ELM-free discharges in NSTX. The characteristics of resistive and ideal edge modes in terms of their eigenfunctions are described in section 4. In section 5 we

Table 1. Overview of analyzed NSTX discharges.

Shot number	Plasma current I_p	Elongation	Triangularity	ELMing
129038	0.8 MA	1.86	0.483	No
132543	1.0 MA	2.10	0.538	Yes
139037	1.2 MA	2.38	0.572	Yes
139047	1.0 MA	2.31	0.626	Yes
141125	0.9 MA	2.46	0.755	No

discuss the influence of finite-Larmor radius effects on PB stability. Finally, section 6 investigates the effect of equilibrium rotation on PB stability in NSTX.

2. Calculation of the peeling-ballooning stability boundary with M3D-C1

2.1. Plasma equilibria

The linear stability simulations are based on kinetic EFIT equilibrium reconstructions [26–28] of NSTX experiments, which in addition to the Grad–Shafranov solution also contain information about density, temperature and rotation profiles of the different particle species. For the ELMing discharges the measurements of the Thomson scattering diagnostics are averaged during the last 20% of the inter-ELM period, to obtain a better spatial resolution for the n_e and T_e profiles [29]. In the ELM-free discharges 129038 and 141125 the averaging is performed over a window of 100 ms centered at 400 ms and 840 ms, respectively. To study the stability thresholds in ELMing scenarios, we choose three typical (often termed ‘narrow pedestal’) H-mode discharges 132543, 139037 and 139047 [14, 30, 31]. These cases exhibit steady type-I ELMs and the availability of good measurements ensures robust equilibrium reconstructions. ELM-free operation in NSTX is achieved in a regime termed ‘wide-pedestal H mode’ (WP H-mode), where evaporative lithium coatings are used to reduce deuterium wall recycling [32]. This results in a wider density pedestal with smaller gradient. Together with changes in anomalous transport the reduction of particle density close to the plasma edge shifts the strong pressure gradient region inwards, which enables ELM-free operation. In this study we consider two WP H-mode cases 129038 (lower single null divertor) and 141125 (double null divertor) [11, 33]. A summary of relevant parameters for the discharges used in this study is shown in table 1.

The plasma profiles for electron density n_e , electron temperature T_e , ballooning parameter α (normalized pressure gradient) [34] and surface-averaged toroidal current density $\langle j_\phi \rangle$ of the considered discharges are shown in figure 1. The pedestal top is located around $\psi_N = 0.9$ in the ELMing cases and around $\psi_N = 0.7$ in the ELM-free cases. The shown n_e and T_e profiles result in a well pronounced pressure pedestal in all cases except 139047, where the pedestal shoulder is very weak, but the normalized pressure α reaches values comparable to the other ELMing discharges. Ion density n_i and temperature T_i are part of the equilibrium reconstruction, but do not enter the stability calculations, as in the MHD model $n_i = n_e$ and T_i is thus determined by the electron profiles and total pressure.

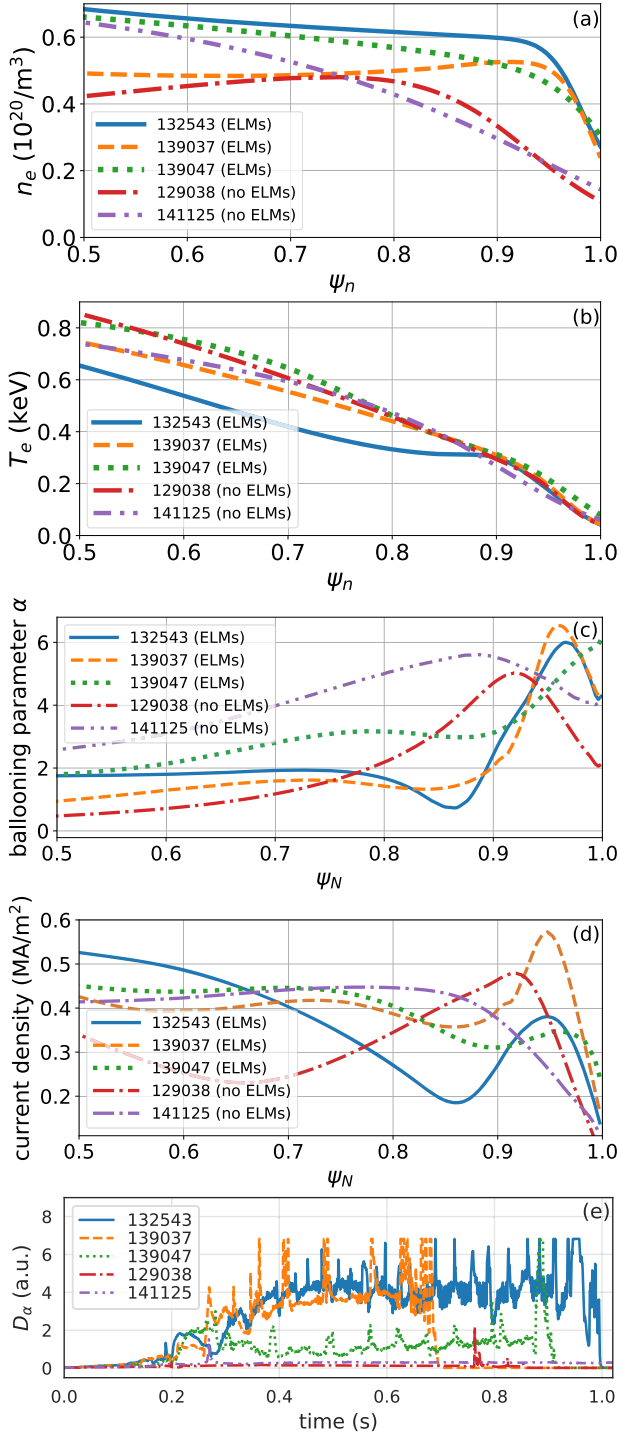


Figure 1. Reconstructed profiles of (a) electron density n_e , (b) electron temperature T_e , (c) ballooning parameter α and (d) toroidal current density j_ϕ as a function of the normalized poloidal flux ψ_N prior to the onset of ELMs. (e) Time trace of divertor D_α .

Figure 1 also shows the divertor D_α emission time trace showing the occurrence of ELMs in discharges 132543, 139037 and 139047.

To compute the stability threshold for PB modes relative to the experimental operational point, we vary the pedestal pressure and the pedestal current density around the original equilibrium reconstruction. This variation is performed with

the VARYPED tool [29], such that the total energy and collisionality remain constant. This provides plasma equilibria with associated kinetic profiles that range up to the last closed flux surface. In order to avoid discontinuities around the separatrix, the profiles for electron density and electron temperature are extended beyond $\psi_N = 1$ by fitting a modified tanh function of the form $c_1[1 - \tanh(c_2(\psi_N - c_3))]$ to the pedestal (c_1 , c_2 and c_3 are free parameters). This keeps the profile within the $\psi_N = 1$ flux surface unchanged while providing a more realistic transition to the open field line region. A solution to the Grad–Shafranov equation is then calculated with M3D-C1 on a high resolution mesh, before linear simulations are performed for each equilibrium. Having interfaced M3D-C1 and VARYPED it is possible to calculate the PB stability boundary in $\alpha - j$ -parameter space using extended-MHD models, and thus determine the influence of individual effects on stability. j denotes the normalized pedestal current density.

2.2. Physical model & numerical approach

The initial value code M3D-C1 implements an extended-MHD model based on the Braginskii equations. In this work we seek to study the impact of plasma resistivity, gyroviscosity and equilibrium rotation, for which two-fluid terms can be neglected. The model is given in terms of the equations

$$\begin{aligned}
 \frac{\partial \varrho}{\partial t} + \nabla \cdot (\varrho \mathbf{u}) &= 0, \\
 \varrho \left(\frac{\partial \mathbf{u}}{\partial t} + \mathbf{u} \cdot \nabla \mathbf{u} \right) &= \mathbf{J} \times \mathbf{B} - \nabla p - \nabla \cdot \Pi, \\
 \frac{\partial p}{\partial t} + \mathbf{u} \cdot \nabla p + \Gamma p \nabla \cdot \mathbf{u} &= (\Gamma - 1) [\eta J^2 - \nabla \cdot \mathbf{q} - \Pi : \nabla \mathbf{u}], \\
 \mathbf{E} &= -\mathbf{u} \times \mathbf{B} + \eta \mathbf{J}, \\
 \mathbf{J} &= \frac{1}{\mu_0} \nabla \times \mathbf{B}, \quad \frac{\partial \mathbf{B}}{\partial t} = -\nabla \times \mathbf{E},
 \end{aligned} \tag{1}$$

where, as usual, \mathbf{B} denotes the magnetic field, p the pressure, ϱ the ion mass density, \mathbf{u} the fluid velocity, \mathbf{J} the current density, \mathbf{E} the electric field, η the resistivity, Π the viscous stress tensor and \mathbf{q} the heat flux density [35]. This system of equations is solved in M3D-C1 using C^1 finite elements [24, 25] on an unstructured triangular mesh. The mesh is generated individually for each equilibrium, and adapted such that the mesh elements align with the flux surfaces having high resolution in the pedestal region and lower resolution in other parts of the computational domain.

Plasma resistivity is calculated according to the Spitzer resistivity model. We take the limit of ideal-MHD to be at 10% of Spitzer resistivity. This is justified as the growth rate remains nearly unchanged as resistivity is lowered further [36]. In a recent study it was shown that the growth rate of PB modes in NSTX scales with resistivity η [22]. A strong dependency of the growth rate on resistivity is found when η is half of the Spitzer value or above. M3D-C1 simulations show that for lower resistivity values the scaling becomes weaker and as

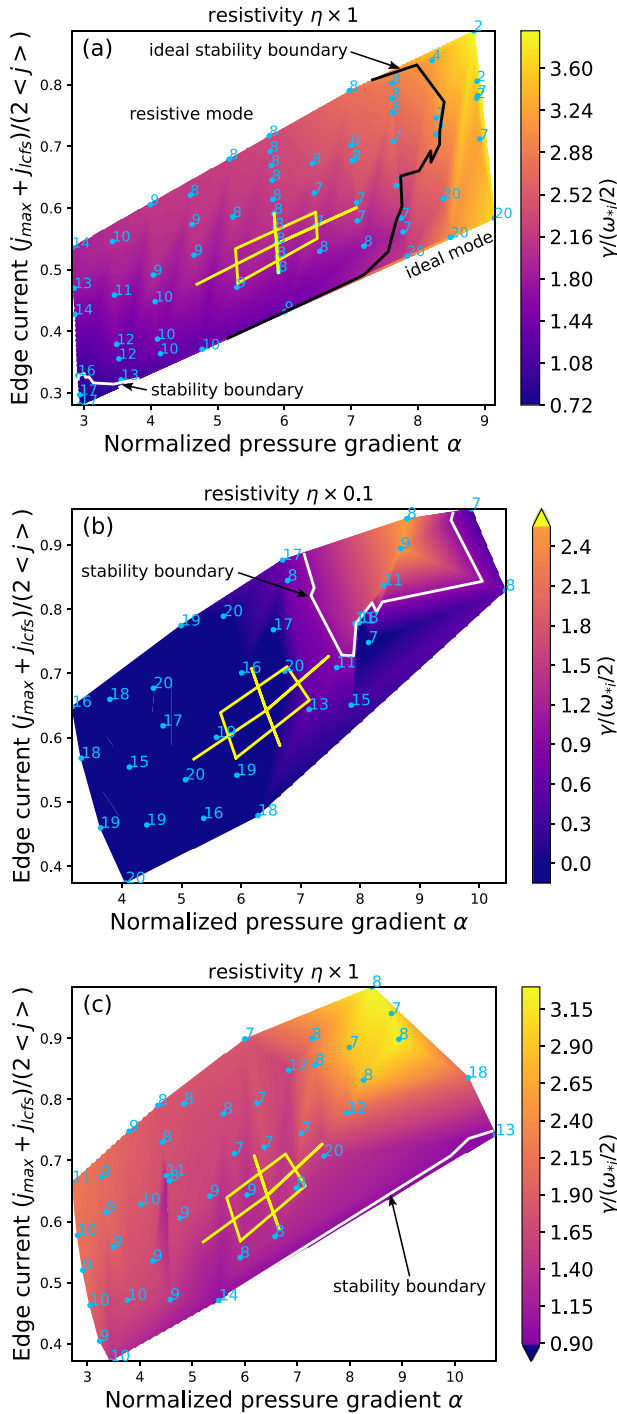


Figure 2. PB stability boundary and normalized growth rate $\gamma/(\omega_{*i}/2)$ of the most unstable mode calculated with M3D-C1 for ELMing discharges. The numbers denote the most unstable toroidal mode at each location, and the solid lines represent the stability boundary at $\gamma/(\omega_{*i}/2) = 1$. (a) 132543, resistive MHD and comparison to ideal MHD limit. (b) 139047, ideal limit. (c) 139047, Spitzer resistivity.

resistivity approaches values of 10% of the Spitzer value and below, the growth rate remains nearly constant.

PB modes are typically observed to rotate in the direction of the ion fluid. For most parts of this study and where not otherwise noted, we therefore choose to set the fluid velocity to the measured toroidal ion rotation $\omega_i = \omega_{E \times B} - \omega_{*m}$,

where ω_{*m} is the main ion diamagnetic rotation frequency. We do not modify the equilibrium to take centrifugal effects into account, as this can cause numerical issues. A detailed analysis of the effect of equilibrium rotation is presented in section 6. In our model the stress tensor Π includes the effect of finite viscosity, which has a direct influence on the growth rate. It is difficult to determine the exact value of viscosity in a fusion plasma. However, by investigating the sensitivity of the PB mode growth rate on viscosity it was determined that within the range of realistic viscosity values the growth rate does not vary strongly in NSTX. Hence, choosing a realistic value for viscosity is expected to result in accurate stability thresholds. For the linear simulations in this paper toroidal mode numbers from $n = 1$ –20 are considered, which are typically the most relevant for PB modes. The mode growth rate is determined as $\gamma = \frac{1}{2} \frac{d}{dt} \ln(E_{\text{kin}})$, where E_{kin} is the plasma kinetic energy. Mode types are characterized in terms of their eigenfunction by evaluating radial and poloidal location, poloidal mode spectrum and driving mechanisms. In the remainder of this paper, $\psi_N = (\psi - \psi_0)/(\psi_1 - \psi_0)$ denotes the normalized poloidal flux. Here, ψ_0 and ψ_1 are the poloidal flux at the magnetic axis and the separatrix, respectively. For the (single fluid) simulations we adopt the same simple model of diamagnetic stabilization as in ELITE [37]. With this normalization the stability boundary is given as $\gamma/(\omega_{*i}/2) = 1$. The plasma is considered stable if $\gamma/(\omega_{*i}/2) < 1$ and unstable if $\gamma/(\omega_{*i}/2) > 1$. Here, γ is the mode growth rate and ω_{*i} is the effective ion diamagnetic frequency in the pedestal. The latter is defined as half of the maximum diamagnetic frequency $\frac{n}{e_i n_i} \frac{dp_i}{d\psi}$ inside the pedestal region (e_i is the ion charge, p_i the ion pressure and ψ the poloidal flux).

3. Resistive scaling of PB modes in NSTX

In the following, we investigate the impact of resistivity on PB modes in NSTX. While a shift of the stability threshold with resistivity was recently reported [22], we now provide more detail of the resistive dependency of PB modes in ELMing discharges. We will also show that ELMing discharges are limited by resistive peeling modes, whereas non-ELMing discharges are located close to an ideal ballooning stability boundary. It is our intention to compare different physical models in multiple discharges. Therefore, in the following, all stability plots showing the same discharge use the same range of the colormap, i.e. contour colors are identical in plots showing the same discharge.

3.1. ELMing discharges

Within the PB model, it is expected that the operational point is located near or inside the unstable domain in $\alpha - j$ parameter space for discharges exhibiting ELMs³. When employing the ideal-MHD model in M3D-C1 computations this is,

³ Whether the experimental point lies inside the unstable domain or near the stability threshold on the stable side depends on the time when the kinetic profiles were obtained relative to the ELM crash. If averaged over a crash, it is probable that it lies slightly in the stable domain. However, for the discharges considered in the presented study the averaging was performed before the ELM crash.

however, not the case as ELMing NSTX discharges are predicted to be stable. This was confirmed in simulations with the ideal-MHD code ELITE [22]. Figure 2 shows the stability boundaries calculated with M3D-C1 in the ideal-MHD limit and with the resistive model for two ELMing discharges. The experimental point (indicated by the cross-hair) is shown relative to the ideal and resistive PB stability boundaries for discharges 132543 and 139047. Figure 2(a) summarizes the result of reference [22] by showing the growth rate calculated with Spitzer resistivity and overlaying the ideal-MHD stability limit. Figures 2(b) and (c) show the results for 139047 in the ideal and resistive model, respectively. When plasma resistivity is introduced a domain of unstable resistive PB modes appears. This shifts the stability boundary considerably to lower values of α and j such that the experimental point appears on the unstable side consistent with the occurrence of ELMs. In both cases a region of ideal instability is found at large values of normalized pedestal pressure α . We will show below that the resistive domain comprises kink-peeling-like modes, whereas the ideal region corresponds to unstable ballooning modes.

A shift of the stability threshold with resistivity is also seen for discharge 139037, which is similar to 139047 but has a larger plasma current ($I_p = 1.2$ MA vs $I_p = 1.0$ MA). The difference to the previous two discharges is that the equilibrium of 139037 is already PB unstable in the ideal limit. With the resistive model the unstable domain expands, but less extensive as in 132543 and 139047. This is shown in figure 3.

We now evaluate the resistive scaling of these novel resistive PB modes and compare it to the well known scalings of other resistive modes. Figure 4 shows the normalized growth rate γ/ω_A for various toroidal modes n as a function of the Lundquist number $S = \tau_R/\tau_A \propto 1/\eta$, where $\tau_R = \mu_0 a^2/\eta$ is the resistive time, a is the minor radius and $\tau_A = 1/\omega_A$ is the Alfvén time. The Alfvén frequency is given as $\omega_A = B_0/(L_0\sqrt{\mu_0 N_0 m_i})$, using $L_0 = 1$ m, $B_0 = 1$ T, $N_0 = 10^{20}$ m⁻³ and m_i being twice the proton mass. As we are interested in comparing the power scalings of γ with S (i.e. the slope of each curve in figure 4) rather than the real growth rates of tearing and infernal modes, the growth rates for tearing modes and resistive infernal modes are normalized to match that of PB modes at the lowest value of S . It is seen that resistive infernal modes exhibit a relatively weak scaling of $S^{-3/13}$ [38] and remain rather unstable even for larger values of S (i.e. less resistive plasmas). In the range $2 \times 10^5 \leq S \leq 10^6$, i.e. when resistivity is larger than Spitzer resistivity, PB modes exhibit a scaling of approximately $S^{-1/2}$ in discharge 132543, which is slower than tearing modes ($S^{-3/5}$). We also calculated the scaling for discharge 139047 where it is roughly $\gamma \propto S^{-0.65}$, which is faster than that of tearing modes. The different scaling laws among these two discharges can be understood by recalling that PB modes can have pressure and current-driven components, which do not necessarily exhibit the same sensitivity to resistivity. As will be shown below, it is the current-driven modes that have a strong sensitivity to resistivity, whereas the pressure-driven part scales only weakly with resistivity. Towards the ideal limit, the resistive PB growth rate exhibits a very steep

drop and eventually crosses the marginal point of stability. The simulations are performed with finite viscosity and this drop is likely associated with the stabilizing effect of finite viscosity on slowly growing modes. M3D-C1 simulations performed with an unrealistically low value of viscosity show weakly unstable modes in the range of $n = 9$ –20. The values for the resistive PB power scalings provided in figure 4 are obtained by fitting a function of the type aS^{-b} to the simulation results before the drop off occurs at larger values of S .

3.2. ELM-free discharges

After finding a strong destabilizing effect of plasma resistivity on PB modes in ELMing cases, we now want to expand the scope of our model by considering ELM-free scenarios in NSTX, namely WP H-mode. This allows us to determine how the different pedestal parameters of WP H-mode affect PB stability and whether resistivity has a similar impact as in the ELMing narrow pedestal cases. Two discharges are considered: 129038 has weaker shaping (elongation $\kappa = 1.86$, triangularity $\delta = 0.483$) and is single null diverted; discharge 141125 has stronger shaping ($\kappa = 2.46$, $\delta = 0.755$), is double null diverted and uses non-axisymmetric magnetic perturbations.

Figure 5 shows the stability boundary for NSTX WP H-mode discharges 129038 and 141125 calculated with M3D-C1 in the ideal-MHD limit and with the resistive model. The operational point of both discharges is located on the stable side independent of the model (ideal or resistive MHD) used, thus indicating stability with respect to ELMs. Contrary to the ELMing cases of section 3.1 no shift of the stability threshold close to the operational point is seen as resistivity is introduced. However, a (smaller) domain of resistive instability appears for large values of edge current density. This provides a consistent picture in terms of PB stability among the two WP H-mode cases. The most unstable part of parameter space is observed at large values of edge pressure and moderate edge current density. This is the domain where ballooning modes can become unstable, as the pressure is destabilizing and magnetic shear is sufficiently large. The closeness of the two operational points to this unstable region indicates that WP H-modes discharges are close to the ballooning stability limit, rather than the kink-peeling limit. 129038 is slightly closer to this limit than 141125. The observed shape of the stability boundary is typical for strongly shaped plasmas [39]. (Note that all of the considered NSTX plasmas exhibit strong shaping compared to many conventional aspect ratio discharges.)

As it is the case for ELMing discharges, by employing a resistive single-fluid MHD model the theoretical calculations locate the experimental points on the correct side of the stability boundary in the considered WP H-mode discharges. The positions of the operational points relative to the stability boundaries indicate that resistivity appears to be important for low-aspect ratio cases that are peeling-limited, i.e. limited by current-driven modes. On the other hand, resistivity appears to be negligible when discharges are pressure-limited, i.e. sit on the ballooning side. A more detailed discussion of the observed resistive and ideal edge modes is presented in the following section.

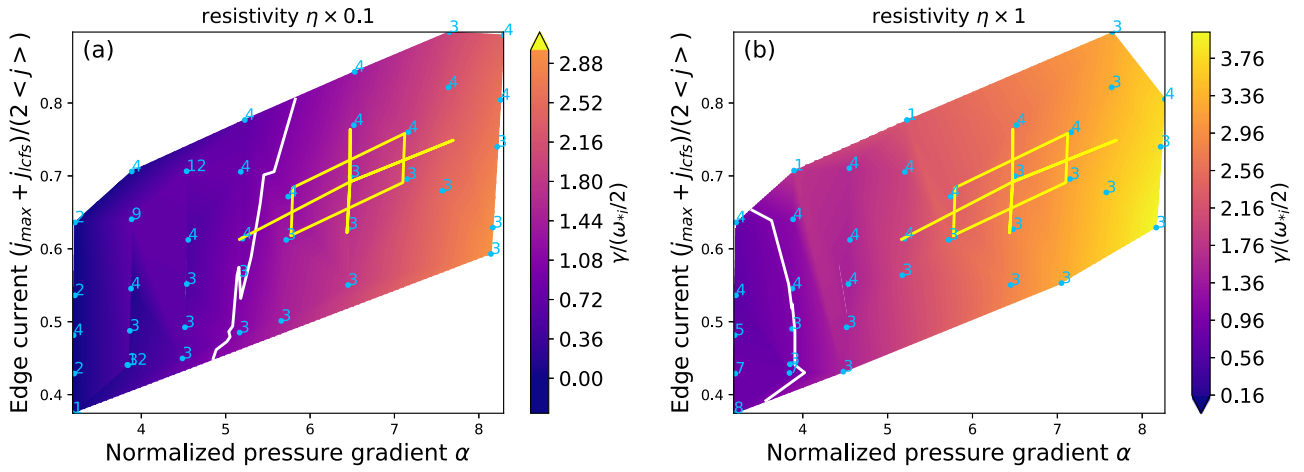


Figure 3. PB stability boundary and normalized growth rate $\gamma/(\omega_{*i}/2)$ of the most unstable mode calculated with M3D-C1 for ELMing discharge 139037. The numbers denote the most unstable toroidal mode at each location. (a) Ideal-MHD limit. (b) Spitzer resistivity.

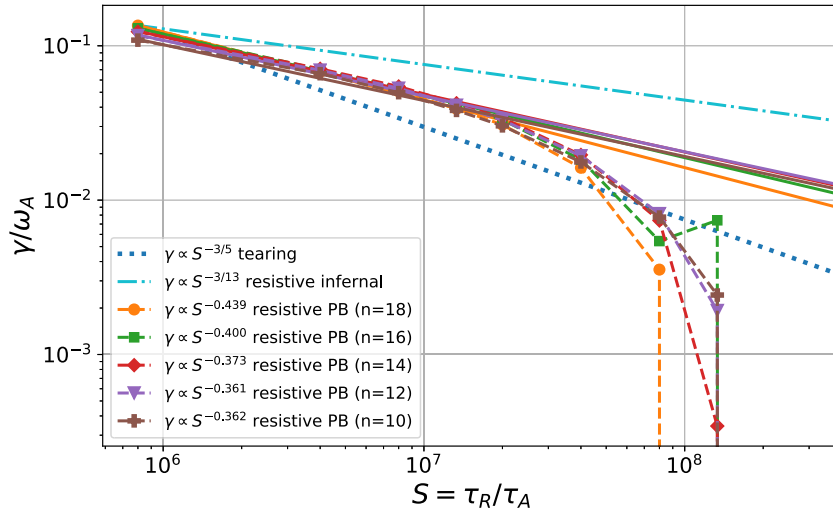


Figure 4. Resistive PB mode growth rate as a function of the Lundquist number S compared with the scaling of tearing modes and resistive infernal modes. The points represent the actual growth rates calculated with M3D-C1, and the solid lines represent a fit through those points at high resistivity.

4. Analysis of mode eigenfunctions

In section 3 it was seen that ELMing discharges are unstable to resistive current-driven modes, whereas ELM-free discharges are located close to an ideal stability threshold. To better understand the differences between resistive and ideal PB modes in NSTX, we now analyze the structure of these modes in terms of their eigenfunction $\xi \propto \delta p = p(t > 0) - p(t = 0)$,⁴ and show how resistivity affects peeling harmonics, but not the ballooning harmonics. For this purpose the poloidal mode spectrum is calculated in PEST coordinates. We also compare the characteristics of these NSTX edge modes to DIII-D results.

⁴To ensure that the eigenfunction corresponds to that of the most unstable mode, $p(t > 0)$ is taken during a phase of constant growth rate, i.e. when the most unstable mode is isolated.

We first inspect the eigenfunctions of resistive and ideal edge modes of ELMing discharge 132543. The left-hand side of figure 6 shows the poloidal spectrum of the most unstable toroidal mode at two locations: in the region of ideal instability at large values of α and in the region of resistive instability at moderate values of α and large values of edge current j . The ideal mode ($n = 20$) shows dominant edge ballooning mode features, i.e. it is a predominantly internal perturbation which peaks well inside the pedestal. Furthermore, the mode has a broad poloidal spectrum and the perturbation is localized at the low-field side. The resistive modes are current-driven as the growth rate scales with j . For the shown resistive mode ($n = 8$) the poloidal harmonics peak close to or at the last closed flux surface, indicating an external kink or peeling mode. In the region of resistive instability the most unstable modes are of lower n as in the domain of ideal ballooning modes (at large α). Similarly, the right-hand side of figure 6 compares the poloidal spectrum of resistive and ideal modes in non-ELMing

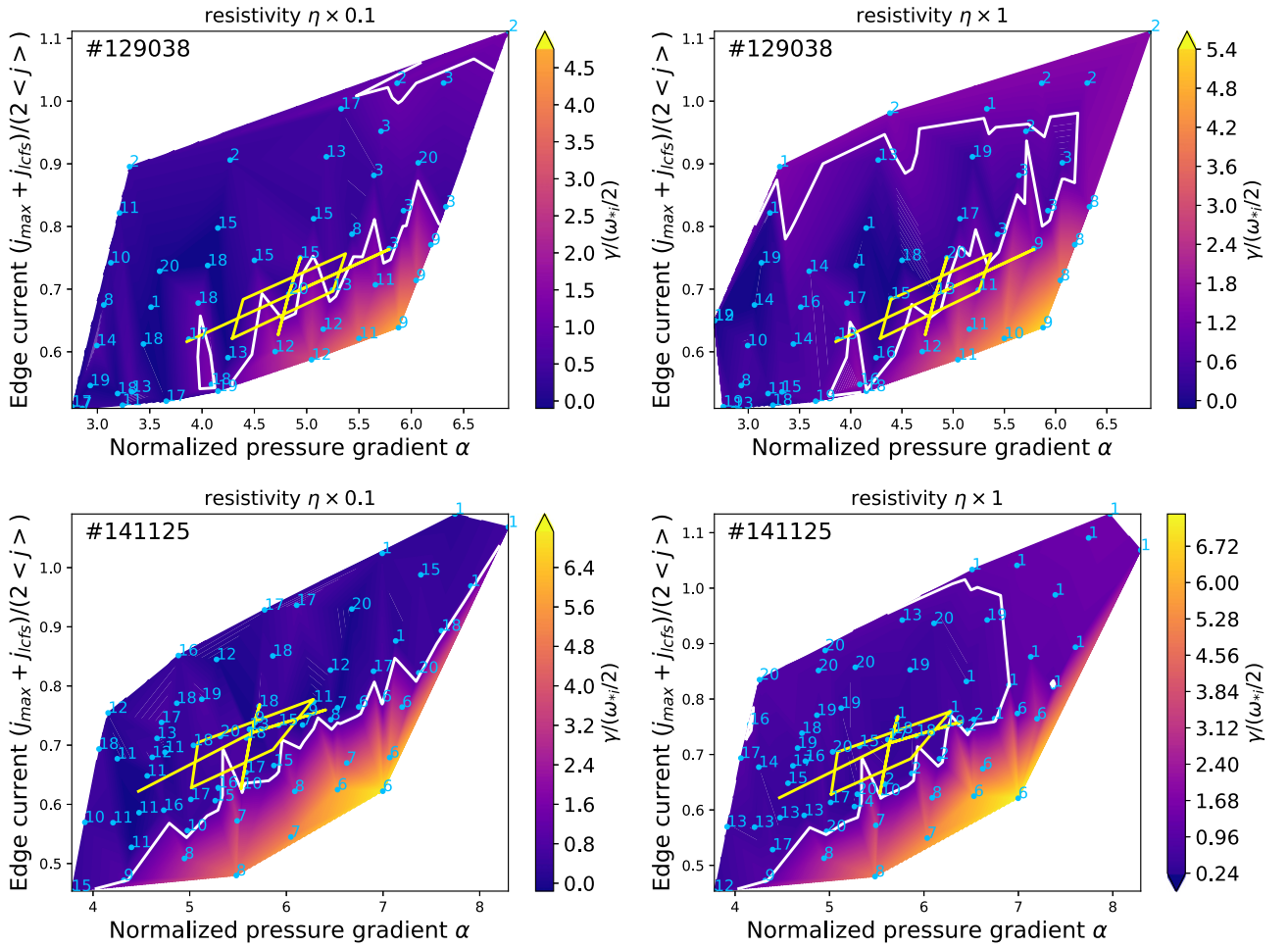


Figure 5. PB stability boundary and normalized growth rate $\gamma/(\omega_{*i}/2)$ of the most unstable mode calculated for NSTX WP H-mode discharges 129038 (top) and 141125 (bottom) in the ideal-MHD limit (left) and with Spitzer resistivity (right).

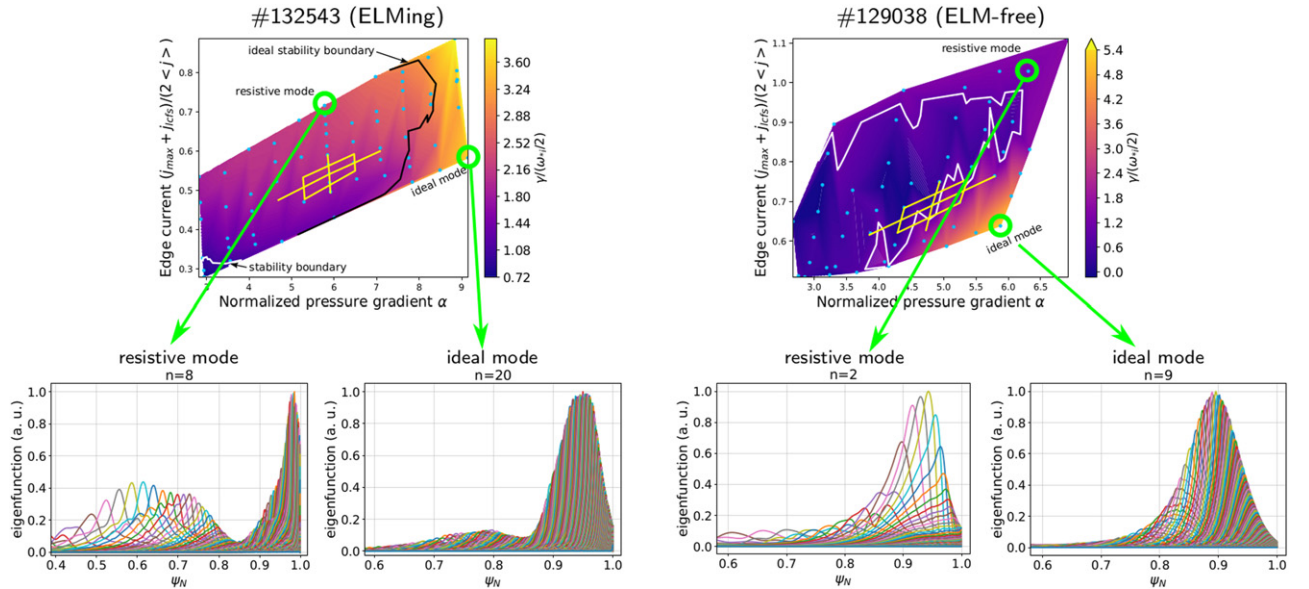


Figure 6. Poloidal spectrum of modes on the resistive kink-peeling side and in the ideal ballooning domain. (Left) for ELMing discharge 132543. (Right) for ELM-free WP H-mode discharge 129038. The eigenfunction of the most unstable mode is shown at the locations indicated by green circles.

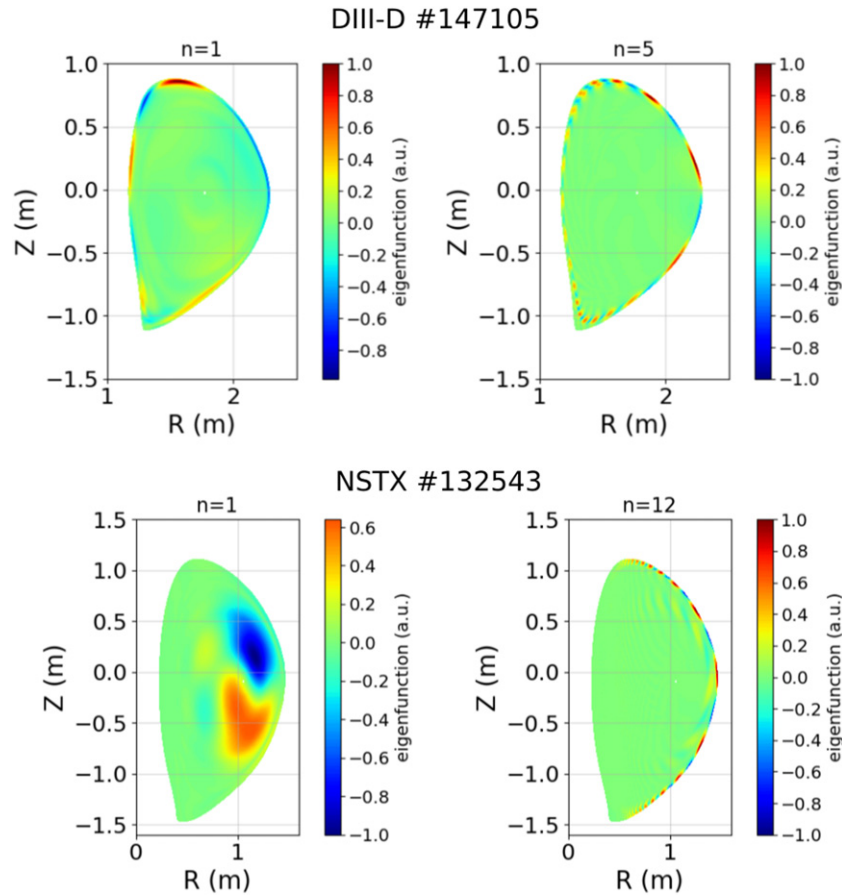


Figure 7. Mode eigenfunctions on the current-driven side of the stability boundary for a discharge in DIII-D (top) and in NSTX (bottom). The most unstable mode in the DIII-D case is $n = 1$, whereas in the NSTX discharge it is $n = 12$.

WP H-mode discharge 129038. As seen in figure 5 the operational point is close to an ideal region of instability. The modes inside this region exhibit similar features as in the ideal region of instability in 132543. The perturbation peaks inside the plasma and is weak at the boundary. Due to the wider pedestal in 129038 the peak of the perturbation is shifted further away from the last closed flux surface compared with 132543. While in both discharges the unstable domain expands when plasma resistivity is considered, the resistive domain in 132543 covers a considerably larger part of parameter space as in 129038 (cf figures 2 and 5). This can be understood in terms of the eigenfunctions of the resistive modes in both cases. In discharge 132543, where the resistive domain extends past the operational point and where resistivity changes the stability picture from stable to unstable, the peeling-component of the mode is dominant throughout the resistive domain. In the ELM-free case 129038, however, the mode in the resistive region is dominantly of ballooning character with somewhat weaker peeling mode components. Peeling and ballooning modes can exhibit a different sensitivity to resistivity, which implies that the composition of coupled PB modes affects the resistive scaling. This can explain why ELMing discharge 139037 shows a weaker scaling with resistivity than the other two ELMing discharges. 139037 is located in a region of unstable coupled PB modes, and only the peeling harmonics are sensitive to resistivity.

The features of PB modes in conventional aspect ratio machines, particularly in DIII-D, are quite similar across a broad spectrum of discharges [40]. While the characteristics of modes on the ballooning side in the NSTX discharges is very similar to ballooning modes in the known large aspect ratio cases, we will now focus on the difference of resistive PB modes in NSTX compared with the well known ideal peeling modes. Typical ideal kink-peeling modes in large aspect ratio have low toroidal mode number n and a rather narrow poloidal spectrum in straight field line coordinates as the perturbation wraps around the poloidal circumference [41, 42]. To compare the properties of kink-peeling modes in NSTX and DIII-D, we choose DIII-D discharge 147105. This discharge was previously investigated [43] in the frame of ideal-MHD, and also used as a benchmark case for M3D-C1 simulations [22]. Since 147105 is a relatively recent discharge compared to other previously analyzed ELMy H-mode discharges in DIII-D, equilibrium reconstruction benefits from better diagnostics measurements. For DIII-D discharge 147105 [43] the M3D-C1 simulations recover the typical characteristics of PB modes in the ideal-MHD limit, as seen in figure 7. For the shown case, which is located on the peeling side, the most unstable toroidal mode is $n = 1$, and the perturbation in the poloidal plane is clearly kink-like. Such low- n modes are not seen in similar studies with the ELITE code, as a result of the underlying expansion in inverse toroidal mode number [7]. The kink-like

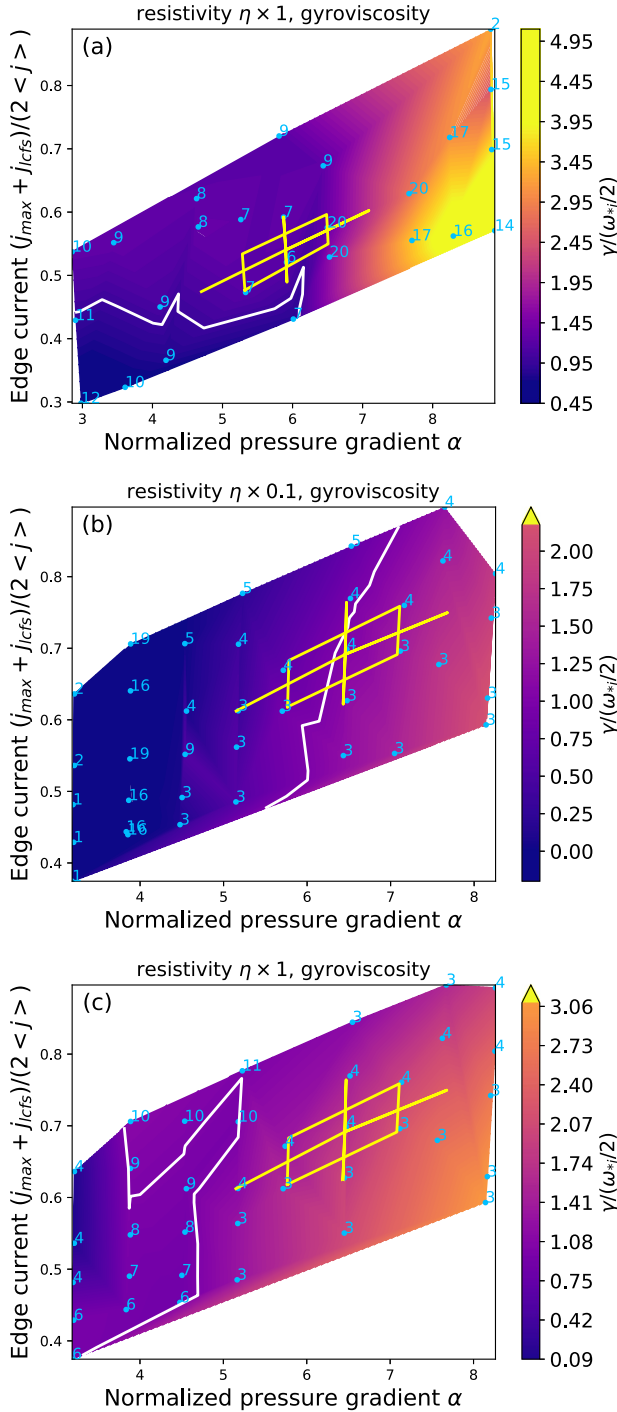


Figure 8. PB stability boundary calculated with the inclusion of gyroviscous stress. (a) 132543, with Spitzer resistivity. (b) 139037, ideal limit. (c) 139037, Spitzer resistivity.

properties are, however, also seen for the $n = 5$ mode and thus consistent with ELITE observations. The characteristics of the resistive current-driven modes in NSTX are different. When unstable modes of low- n are seen on the peeling side, these modes correspond to a mode in the plasma core and ξ in the pedestal is weak. Such modes are not associated with ELMs and hence not considered in the frame of the PB model. An example is seen on the bottom of figure 7, where the $n = 1$ mode is localized in the core and the most unstable mode is

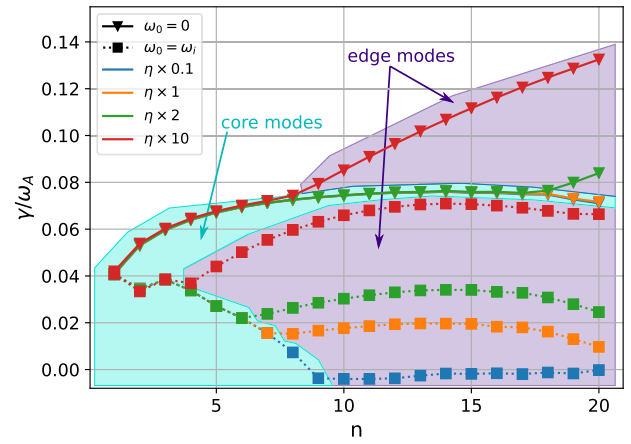


Figure 9. Comparison of normalized growth rate γ/ω_A as a function of the toroidal mode number n without equilibrium rotation and with initial ion rotation for NSTX discharge 132543 with multiple values of plasma resistivity. In the turquoise area the most unstable mode is localized in the core, whereas in the two purple regions edge modes are dominant.

$n = 12$ with a strong perturbation inside the pedestal. This is typical for external kink/peeling modes, yet the perturbation is localized on the low field side, indicating a sensitivity to field line curvature, a typical feature of ballooning modes. It should be noted that NSTX discharges exhibit strong shaping and low-aspect ratio, conditions that contribute to poloidal mode coupling due to toroidicity [44]. Since both, pressure and current density, provide driving forces for instabilities in the plasma edge, it is not unusual that the observed PB modes show features of peeling and also ballooning modes.

5. Finite-Larmor-radius effects

Finite-Larmor-radius stabilization can be represented in MHD models in terms of modifications to the stress tensor and Ohm's law [45]. Oftentimes MHD codes use the gyroviscous cancellation where $\nabla \cdot \Pi \approx -n \mathbf{v}_* \cdot \nabla \mathbf{v}$ to include the diamagnetic drift and v_* is taken to be the diamagnetic drift velocity. So far, in our model diamagnetic effects have been considered in terms of the growth rate normalization. We now investigate the effect of gyroviscosity, which enters the model directly via the gyroviscous-stress tensor in equation (1) and avoids the approximation made by the gyroviscous cancellation. In our model FLR effects are represented via the terms containing Π in equation (1) but not in Ohm's law. FLR effects are fully implemented only in the two-fluid model. Details about the implementation of the gyroviscous stress in M3D-C1 can be found in reference [46]. We note in passing that unlike fluid viscosity gyroviscous stresses are perpendicular to the fluid velocity. Figure 8 shows stability thresholds with the additional effect of gyroviscosity for ELMI discharges 132543 (Spitzer resistivity) and 139037 (Spitzer resistivity and ideal-MHD limit). It is seen that gyroviscosity has a moderate stabilizing effect that moves the stability boundary closer to the experimental point when compared with the models that neglect gyroviscous effects in figures 2 and 3, respectively. In

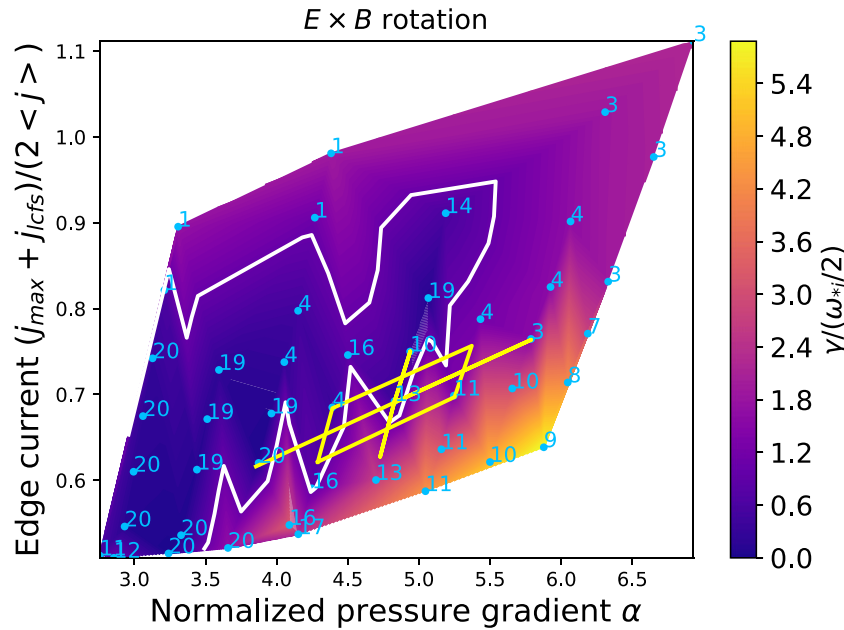


Figure 10. PB stability boundary and normalized growth rate $\gamma/(\omega_{*i}/2)$ of the most unstable mode calculated for NSTX discharge 129038 using equilibrium rotation based on the measured $\mathbf{E} \times \mathbf{B}$ rotation profile.

this ‘standard’ resistive single-fluid model employed above, the experimental point lies deep inside the unstable region, and it should be expected that a plasma would have produced an ELM already before reaching this point. When including the effect of gyroviscosity, the threshold moves closer to the experimental point, provided that the threshold is still determined by the condition that $\gamma = \omega_{*i}/2$. It is questionable whether this choice of threshold is justified for a model that includes gyroviscosity, however, given that the $\omega_{*i}/2$ threshold is intended to represent the value of γ below which diamagnetic effects (including gyroviscosity) would fully stabilize the ideal-MHD PB mode. In a model that includes diamagnetic effects, one might conclude that the threshold $\gamma = 0$ would be the appropriate one. In fact, simulations that include resistivity find small ($\gamma\tau_A \ll 1$) positive values of γ over a much broader range of conditions than where ELMs are actually observed, and therefore there is evidently a threshold for γ below which these slow-growing instabilities do not result in ELMs, either due to saturation at small amplitudes or stabilization by additional physics. These questions should be investigated through calculations using more complete physics models and careful validation against experiment.

6. Effect of plasma rotation on PB modes in NSTX

Ideal-MHD PB stability calculations in conventional aspect ratio devices are typically carried out without plasma equilibrium rotation, as its effect on the growth rates is negligible [47]. It is, however, not clear if this is also true for resistive PB modes in low-aspect ratio plasmas [48]. M3D-C1 is capable of processing a variety of measured rotation profiles, including $\mathbf{E} \times \mathbf{B}$ rotation, and rotation of electron and ion species. In the following, we will discuss to what degree equilibrium rotation is important when assessing edge stability limits in NSTX. To

include the effect of rotation in M3D-C1, the initial fluid velocity $\mathbf{v}(t=0)$ is set based on the measured rotation values, but the equilibrium is calculated without centrifugal effects as this can cause numerical difficulties.

We now calculate the growth rate γ without equilibrium rotation, and demonstrate that in the considered NSTX cases equilibrium rotation can suppress ideal-MHD modes located in the core, and thus helps isolate edge modes. This is illustrated in figure 9, which shows the linear growth rate in discharge 132543 as a function of the toroidal mode number n for multiple values of plasma resistivity without equilibrium rotation and with main ion rotation. The resistivity scale factors are chosen to illustrate the dependence of γ on resistivity and do not necessarily have a physical meaning. In the calculations with zero equilibrium rotation an ideal mode localized in the plasma core ($\psi_N < 0.6$) is strongly unstable. An example of such a low- n core mode is seen in figure 7, where the perturbation peaks around $\psi_N = 0.4$. It is not clear if at low- n independent edge modes occur as well, since the edge perturbation is rather weak and could be due to coupling with the main mode in the core. When equilibrium rotation is considered based on the measured main ion rotation profile, ideal core modes become suppressed at $n \approx 4-10$ (depending on resistivity) and edge modes are seen. For η well above the Spitzer value plasma rotation appears to be stabilizing on edge modes. However, this cannot be said about edge modes at lower resistivity as edge modes are obscured by more unstable core modes. At low- n the core modes persist and coexist with weak edge modes. However, for the calculation of the PB stability boundary these low- n modes are not relevant as higher- n modes are the most unstable.

We also want to compare the PB stability boundary calculated with rotation profiles based on the measured $\mathbf{E} \times \mathbf{B}$ rotation in order to increase confidence in the results. For this

comparison we choose discharge 129038 as it features a clear ideal (ballooning) stability limit and also a resistive stability limit. Figure 10 shows the PB stability boundary calculated with equilibrium $\mathbf{E} \times \mathbf{B}$ rotation. The stability boundary closely resembles that of the simulations with equilibrium ion rotation of figure 5. While equilibrium rotation can suppress ideal core modes found in some NSTX discharges, a considerable effect on PB stability cannot be inferred at realistic values of resistivity.

7. Conclusions





A study of PB stability thresholds in ELMing and ELM-free NSTX discharges using extended-MHD models was presented. It is found that plasma resistivity is crucial to the stability of PB modes in NSTX, and that other non-ideal effects can be moderately stabilizing. ELMing NSTX discharges are found to be predominantly limited by current-driven peeling modes. Plasma resistivity can considerably expand the peeling-unstable domain in these discharges, such that the experimental point is correctly located on the unstable side. One ELMing case (139037) was found to be unstable to coupled PB modes, and the scaling with resistivity is somewhat weaker. On the other hand, wide-pedestal H-mode discharges sit inside the stable domain close to the ballooning stability threshold in both, the ideal-MHD limit and the resistive model. This difference is understood by investigating the mode properties of the ideal and resistive modes. Analysis of the mode eigenfunctions implies that resistivity destabilizes only the kink-peeling harmonics, while the ballooning harmonics are ideal. The ideal modes are localized inside the pedestal, whereas the resistive modes peak at the plasma boundary, which is characteristic of kink-peeling modes. Compared with ideal peeling modes in DIII-D, these resistive modes have a larger toroidal mode number and a broader poloidal spectrum. The study found that gyroviscosity has a moderate stabilizing effect and can result in more accurate stability thresholds. Equilibrium rotation most notably suppresses core modes, but also appears to stabilize edge modes at large values of resistivity. Our resistive single-fluid model including gyroviscous stress is capable of capturing the PB stability limits in ELMing as well as ELM-free discharges. This result will contribute to the development of a high-fidelity predictive pedestal structure model that is applicable to a broader range of tokamaks, particularly NSTX. It is unclear whether the destabilization of resistive kink-peeling modes is a result of spherical tokamak geometry or alterations to the plasma profiles due to Li coating. This is currently under investigation.

Acknowledgments

The authors thank Devon Battaglia, Walter Guttenfelder and Tom Osborne for useful discussions. This research used resources of the National Energy Research Scientific Computing Center, which is supported by the Office of Science

of the U.S. Department of Energy under Contract No. DE-AC02-05CH11231. This work was supported by the U.S. Department of Energy under contracts DE-AC02-09CH11466, DE-FC02-04ER54698 and the Department of Energy early career research program. The United States Government retains a non-exclusive, paid-up, irrevocable, world-wide license to publish or reproduce the published form of this manuscript, or allow others to do so, for United States Government purposes.

ORCID iDs

A. Kleiner  <https://orcid.org/0000-0002-5800-8027>
 N.M. Ferraro  <https://orcid.org/0000-0002-6348-7827>
 A. Diallo  <https://orcid.org/0000-0002-0706-060X>
 R. Maingi  <https://orcid.org/0000-0003-1238-8121>

References

- [1] Wagner F. et al 1982 *Phys. Rev. Lett.* **49** 1408–12
- [2] Zohm H. 1996 *Plasma Phys. Control. Fusion* **38** 105–28
- [3] Federici G., Loarte A. and Strohmayer G. 2003 *Plasma Phys. Control. Fusion* **45** 1523–47
- [4] Leonard A.W. 2014 *Phys. Plasmas* **21** 090501
- [5] Connor J.W., Hastie R.J., Wilson H.R. and Miller R.L. 1998 *Phys. Plasmas* **5** 2687–700
- [6] Wilson H.R., Cowley S.C., Kirk A. and Snyder P.B. 2006 *Plasma Phys. Control. Fusion* **48** A71–84
- [7] Snyder P.B. et al 2002 *Phys. Plasmas* **9** 2037–43
- [8] Wilson H.R., Snyder P.B., Huysmans G.T.A. and Miller R.L. 2002 *Phys. Plasmas* **9** 1277–86
- [9] Saarelma S., Hender T.C., Kirk A., Meyer H. and Wilson H.R. (MAST Team) 2006 *Plasma Phys. Control. Fusion* **49** 31–42
- [10] Knolker M., Osborne T., Belli E., Henderson S., Kirk A., Kogan L., Saarelma S. and Snyder P.B. 2021 *Nucl. Fusion* **61** 046041
- [11] Maingi R. et al (the NSTX Research Team) 2009 *Phys. Rev. Lett.* **103** 075001
- [12] Boyle D.P., Maingi R., Snyder P.B., Manickam J., Osborne T.H., Bell R.E. and LeBlanc B.P. 2011 *Plasma Phys. Control. Fusion* **53** 105011
- [13] Sontag A.C. et al 2011 *Nucl. Fusion* **51** 103022
- [14] Diallo A. et al 2011 *Nucl. Fusion* **51** 103031
- [15] Diallo A. et al 2013 *Nucl. Fusion* **53** 093026
- [16] Peeters A.G. 2000 *Plasma Phys. Control. Fusion* **42** B231–42
- [17] Peng Y.-K.M. and Strickler D.J. 1986 *Nucl. Fusion* **26** 769–77
- [18] Canik J.M. et al 2013 *Nucl. Fusion* **53** 113016
- [19] Strauss H.R. 1981 *Phys. Fluids* **24** 2004–9
- [20] Sykes A., Bishop C.M. and Hastie R.J. 1987 *Plasma Phys. Control. Fusion* **29** 719–27
- [21] Xia T.Y., Xu X.Q. and Xi P.W. 2013 *Nucl. Fusion* **53** 073009
- [22] Kleiner A., Ferraro N.M., Diallo A. and Canal G.P. 2021 *Nucl. Fusion* **61** 064002
- [23] Jardin S.C., Ferraro N., Breslau J. and Chen J. 2012 *Comput. Sci. Discovery* **5** 014002
- [24] Jardin S.C. 2004 *J. Comput. Phys.* **200** 133–52
- [25] Jardin S.C., Breslau J. and Ferraro N. 2007 *J. Comput. Phys.* **226** 2146–74
- [26] Lao L.L., St. John H., Stambaugh R.D., Kellman A.G. and Pfeiffer W. 1985 *Nucl. Fusion* **25** 1611–22

- [27] Lao L.L., John H.E.S., Peng Q., Ferron J.R., Strait E.J., Taylor T.S., Meyer W.H., Zhang C. and You K.I. 2005 *Fusion Sci. Technol.* **48** 968–77
- [28] Meneghini O. et al 2015 *Nucl. Fusion* **55** 083008
- [29] Osborne T.H., Snyder P.B., Burrell K.H., Evans T.E., Fenstermacher M.E., Leonard A.W., Moyer R.A., Schaffer M.J. and West W.P. 2008 *J. Phys.: Conf. Ser.* **123** 012014
- [30] Maingi R. et al 2017 *Fusion Eng. Des.* **117** 150–6
- [31] Coury M., Guttenfelder W., Mikkelsen D.R., Canik J.M., Canal G.P., Diallo A., Kaye S., Kramer G.J. and Maingi R. 2016 *Phys. Plasmas* **23** 062520
- [32] Maingi R. et al 2015 *J. Nucl. Mater.* **463** 1134–7
- [33] Battaglia D.J. et al 2020 *Phys. Plasmas* **27** 072511
- [34] Miller R.L., Chu M.S., Greene J.M., Lin-Liu Y.R. and Waltz R.E. 1998 *Phys. Plasmas* **5** 973–8
- [35] Breslau J., Ferraro N. and Jardin S. 2009 *Phys. Plasmas* **16** 092503
- [36] Ferraro N.M., Jardin S.C. and Snyder P.B. 2010 *Phys. Plasmas* **17** 102508
- [37] Snyder P.B., Groebner R.J., Hughes J.W., Osborne T.H., Beurskens M., Leonard A.W., Wilson H.R. and Xu X.Q. 2011 *Nucl. Fusion* **51** 103016
- [38] Brunetti D., Graves J.P., Cooper W.A. and Wahlberg C. 2014 *Plasma Phys. Control. Fusion* **56** 075025
- [39] Snyder P.B. et al 2009 *Nucl. Fusion* **49** 085035
- [40] Burrell K.H., Osborne T.H., Snyder P.B., West W.P., Fenstermacher M.E., Groebner R.J., Gohil P., Leonard A.W. and Solomon W.M. 2009 *Nucl. Fusion* **49** 085024
- [41] Kleiner A., Graves J.P., Cooper W.A., Nicolas T. and Wahlberg C. 2018 *Nucl. Fusion* **58** 074001
- [42] Kleiner A., Graves J.P., Brunetti D., Cooper W.A., Medvedev S., Merle A. and Wahlberg C. 2019 *Plasma Phys. Control. Fusion* **61** 084005
- [43] Wade M.R. et al 2015 *Nucl. Fusion* **55** 023002
- [44] D’Ippolito D.A. 1980 *Plasma Phys.* **22** 1091–107
- [45] Roberts K.V. and Taylor J.B. 1962 *Phys. Rev. Lett.* **8** 197–8
- [46] Ferraro N.M. and Jardin S.C. 2006 *Phys. Plasmas* **13** 092101
- [47] Snyder P.B. et al 2007 *Nucl. Fusion* **47** 961–8
- [48] Xi P.W., Xu X.Q., Wang X.G. and Xia T.Y. 2012 *Phys. Plasmas* **19** 092503